ACS APPLIED MATERIALS & INTERFACES

www.acsami.org
Research Article

Protein Stacking on the APTES-Functionalized Pyrochlore $Bi_2Ru_2O_7$ Clusters for Ultrasensitive and Selective Immunosensing

Nikola Tasić,* Nika Vranešič, Dino Metarapi, Kristina Mervič, Milan Žunić, Aleksandra Dapčević, Matjaž Finšgar, and Samo B. Hočevar*

Cite This: *ACS Appl. Mater. Interfaces* 2025, 17, 10792−10801

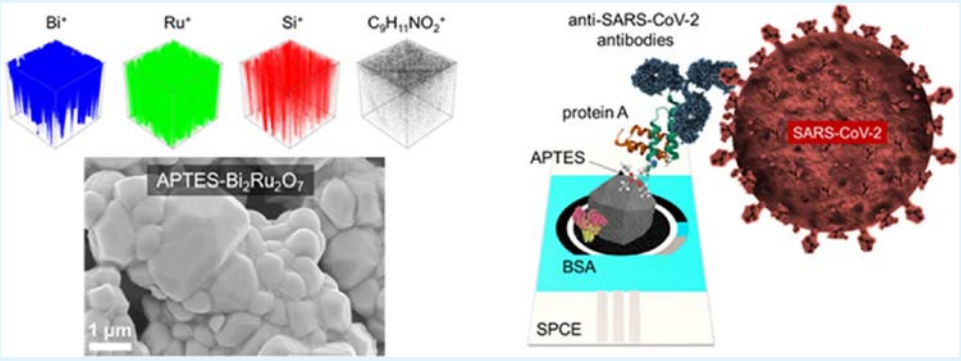

ABSTRACT: With their unique physicochemical properties, such as metallic-like conductivity, favorable (electro)catalytic properties, electrochemical stability, and ease of functionalization, pyrochlores have found applications in various fields such as solid oxide fuel cells, batteries, thick film resistors, and temperature sensors; however, there are no reports on their application in electrochemical immunosensing. In this study, we exploited the (electro)catalytic nature and stability of the pyrochlore $Bi_2Ru_2O_7$ clusters silanized with (3-aminopropyl)triethoxysilane (APTES) to demonstrate their potential for the effective stacking of functional proteins. Characterization of the clusters by XPS disclosed a dual environment of Bi, also indicating the presence of Bi_2O_3 alongside APTES-$Bi_2Ru_2O_7$ clusters and, importantly, the predominant involvement of pyrochlore moieties in subsequent protein stacking. After stacking protein A and antibodies, the immunosensor revealed a nearly interference-free operation, high sensitivity, a detection limit of 118 fM SARS-CoV-2 spike protein, and operation in a wide examined concentration range of 10^{-5}−10^{-1} μg mL^{-1} with an r^2 of 0.98. In combination with a short incubation time of 30 min, the pyrochlore-based immunosensor provides a solid platform for future point-of-need applications.

KEYWORDS: *$Bi_2Ru_2O_7$ pyrochlore, APTES, SARS-CoV-2, spike protein, immunosensor, electrochemical, impedimetric*

INTRODUCTION

Since the early works,[1,2] pyrochlore-type compounds of general formula $A_2Ru_2O_{7-\delta}$ (A = Pb, Bi) have attracted notable attention considering the energy-related and electronic applications, such as temperature sensors[3] and thick film resistors.[4−6] Of particular interest is bismuth-ruthenate ($Bi_2Ru_2O_7$), which exhibits an effective bifunctional (electro)-catalytic nature for both oxygen evolution reaction (OER) and oxygen reduction reaction (ORR), and it is characterized by a highly stable structure during electrocatalysis,[7] thus making it a perfect candidate for sodium-air batteries.[8] Its electrical and catalytic properties, similar to those of RuO_2, have nominated it as a cathode material in solid oxide fuel cells.[9,10] In addition, a recent report indicates its use in a nanocomposite with Pd particles and $BiVO_4$ for the photocatalytic degradation of trichloroethylene.[11] However, despite its apparent catalytic superiority and excellent stability, scrutinized in a recent study,[7] the application of pyrochlores in sensor development is almost nonexistent. A solid electrolyte sensor using a sodium superionic conductor, i.e., NASICON, and a pyrochlore-type oxide ($Pb_2Ru_{1.9}V_{0.1}O_{7-\delta}$) electrode was found promising for the potentiometric sensing of gaseous NO and NO_2 at 400 °C,[12] being the only thus far reported pyrochlore-based electrochemical sensor.

Electrochemical immunosensors have proven highly effective due to their enhanced sensitivity, selectivity, cost-effectiveness, quick response, and suitability for on-site applications.[13−15]

Received: October 16, 2024
Revised: December 19, 2024
Accepted: January 25, 2025
Published: February 6, 2025

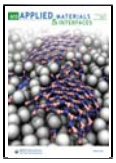

https://doi.org/10.1021/acsami.4c17869
ACS Appl. Mater. Interfaces 2025, 17, 10792−10801

The SARS-CoV-2 virus has exemplified the critical importance and necessity of effective point-of-care immunosensors and assays for rapid and accurate detection in combating and controlling infectious disease outbreaks. Various types of (nano)materials have been explored for this purpose, including metallic nanoparticles,[16] metal oxides,[17] carbon-based nanomaterials,[18] 2D-layered MXenes,[19] nanocomposites,[20] etc. Alternatively, SARS-CoV-2 can be detected via colorimetric assays,[21] lateral flow assays,[22] molecular detection methods such as PT−PCR,[23] LAMP,[24] or CRISPR-based detection.[25]

Here, we show for the first time how (electro)catalytic and silanized APTES-$Bi_2Ru_2O_7$ clusters deposited on a screen-printed carbon electrode (SPCE) are ideally suited for further immobilization of the biological recognition element, i.e., the anti-SARS-CoV-2 antibodies, and enable highly sensitive impedimetric detection of the SARS-CoV-2 spike protein. The silanization with APTES was carried out to enable the binding of the pyrochlore clusters to the −OH groups of the HNO_3-pretreated supporting electrode while enabling, on the other side, cross-links to protein A via glutaraldehyde (GA). GA is used as a cross-linking agent due to its high reactivity toward amino, hydroxyl, and carboxyl groups, whereas protein A provides a site-directed end-on fab-up immobilization of the anti-SARS-CoV-2 antibodies via their Fc fragments. In addition, the interference-free operation of the immunosensor was confirmed in the selectivity study with potential interferents such as the MERS, HCoV-OC43, HCoV-HKU1, HCoV-NL63, and HCoV-229E spike proteins.

RESULTS AND DISCUSSION

Pyrochlore Characterization. The powder XRD pattern (Figure 1) of a synthesized $Bi_2Ru_2O_7$ sample can be indexed as

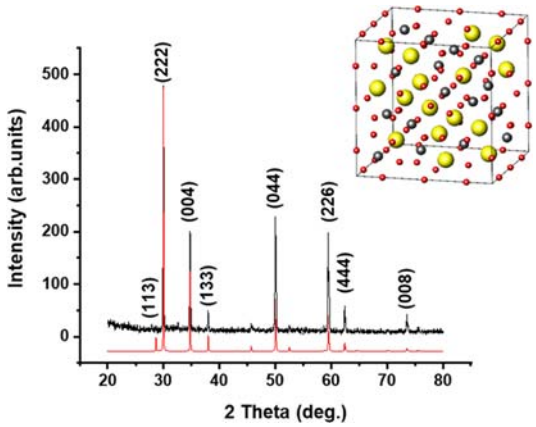

Figure 1. XRD pattern of the synthesized $Bi_2Ru_2O_7$ powder. The black spectrum corresponds to synthesized $Bi_2Ru_2O_7$ particles, while the red spectrum corresponds to the powder diffraction pattern for dibismuth(III) diruthenate(IV), classified under ICSD #78114.[26] The inset shows the theoretical crystal structure of the cubic $Bi_2Ru_2O_7$, with Bi atoms in yellow, Ru atoms in gray, and O atoms in red.

cubic pyrochlore-type oxides (space group $Fd\bar{3}m$). There are two crystallographic cation sites in the $Bi_2Ru_2O_7$ crystal structure, i.e., 16d and 16c (inset of Figure 1); the Bi atom surrounded by eight O atoms in a distorted dodecahedron is located at 16d, while RuO_6 octahedra occupy 16c. The observed diffraction peaks at 27.9, 30.0, 34.8, 38.0, 50.0, 59.5, 62.4, and 73.5° are assigned to (113), (222), (004), (133), (044), (226), (444), and (008) crystallographic planes, respectively.[8] No prominent peaks in the powder XRD pattern corresponding to other phases or oxides were observed; this was also supported later by EDX analysis and the observed ratio between the metallic centers. The crystallite size of the synthesized material was 66.1 nm, calculated by Scherrer's equation.

Insights into the structure of APTES-$Bi_2Ru_2O_7$ clusters were obtained by field-emission scanning electron microscopy (FE-SEM) analysis, as shown in Figures 2 and S2. The submicrometer particles exhibit an irregular shape, resembling a rhombicuboctahedral structure, a polyhedron with triangular, square, and rectangular faces.

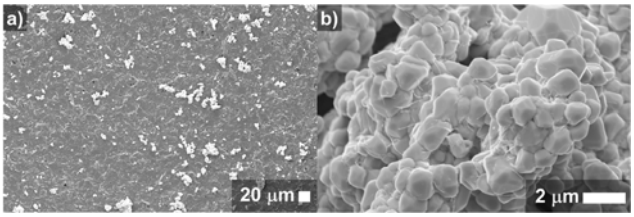

Figure 2. FE-SEM images of an SPCE modified with pyrochlore clusters. (a) APTES-$Bi_2Ru_2O_7$ clusters on the SPCE (concentration of the drop-casting solution was 5 mg mL^{-1} in dH_2O), and (b) APTES-$Bi_2Ru_2O_7$ cluster at high magnification. The morphology analyses carried out on the bare SPCE are presented in Figure S1.

We also performed EDX analysis on the APTES-$Bi_2Ru_2O_7$ clusters, and the corresponding results are shown in Figure 3. Carbon and silicon are attributed to APTES as aminosilanes with a gross molecular formula of $C_9H_{23}NO_3Si$. Highly magnified images of APTES-$Bi_2Ru_2O_7$ clusters revealed superficial features resembling a spider web, likely originating from APTES (Figure S2).

The atomic ratio between Bi and Ru is stoichiometric with respect to the theoretical formula of $Bi_2Ru_2O_7$, with an almost perfect match of the expected and measured atomic percentages, i.e., 18.2 vs 17.4 at. % for Bi and 18.2 vs 17.3 at. % for Ru, respectively. A slightly lower percentage of oxygen compared to the theoretical value is a common and highly desirable feature of pyrochlore structures, indicating the presence of oxygen vacancies.[27] The corresponding atomic and weight distributions are shown as graphs in Figure S3.

Electrochemical Studies of the Pyrochlore-Modified Electrode. The development of immunosensors requires the integration of building blocks that are electrochemically stable and reproducible in the standard biocompatible media of confirmed physiological relevance. We carried out cyclic voltammetric (CV) and square-wave voltammetric (SWV) characterization of unmodified and APTES-modified $Bi_2Ru_2O_7$ clusters in (i) 0.1 M KCl (pH = 7.0) and (ii) 1.0 mM $[Fe(CN)_6]^{3-/4-}$ in 0.1 M KCl deposited on the substrate SPCE. The electrochemical behavior of the deposited pyrochlore $Bi_2Ru_2O_7$ clusters in a redox-free medium, i.e., in 0.1 M KCl, revealed a dual (electro)catalytic nature described by OER in the anodic region and ORR in the cathodic region (Figure S4). In addition, the ruthenium ions' irreversible and discrete surface oxidation was observed in the anodic region, with a peak potential at ca. +0.6 V during the first CV potential scan. It was observed that although multivalent metallic centers are present in the structure of the (electro)catalytic material, no distinct internal redox system was present after the first CV scan. Notably, due to the absence of APTES, the adhesion of

https://doi.org/10.1021/acsami.4c17869
ACS Appl. Mater. Interfaces 2025, 17, 10792−10801

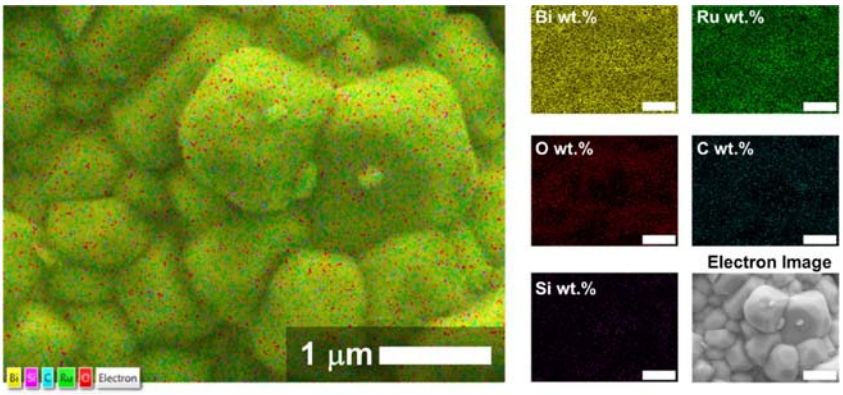

Figure 3. Elemental distribution in APTES-$Bi_2Ru_2O_7$ clusters. The size bars on the right-side micrographs correspond to 1 μm.

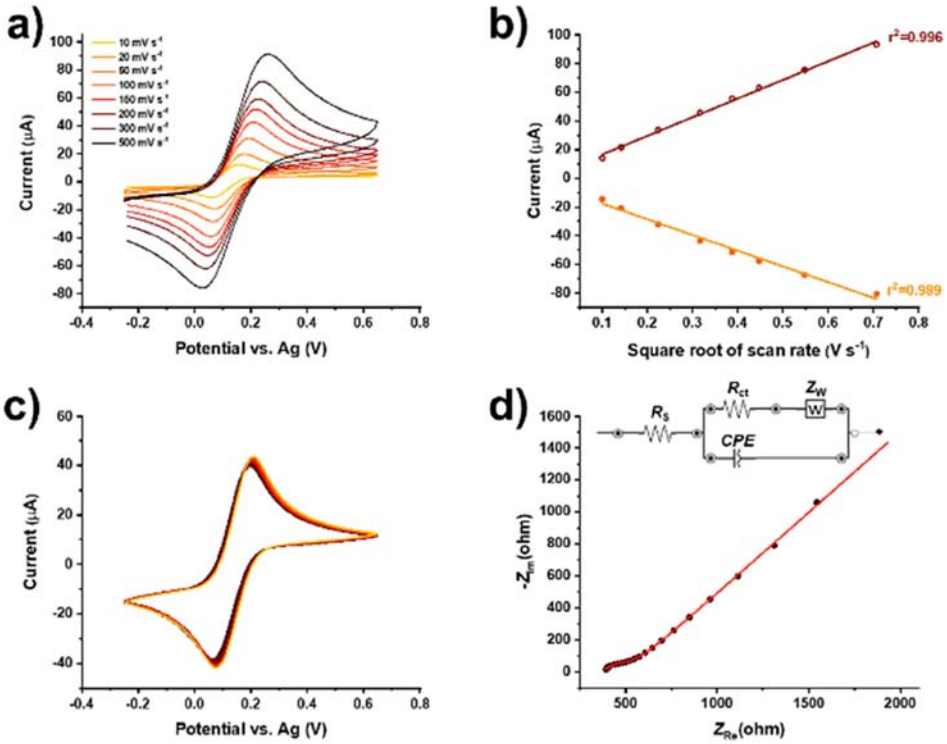

Figure 4. Electrochemical characterization of APTES-$Bi_2Ru_2O_7$ cluster-modified SPCE in relevant physiological media. (a) CV measurements using different scan rates and (b) the corresponding oxidation and reduction peak currents with respect to the square root of the scan rate, (c) 30 consecutive CVs, and (d) EIS measurement in 1.0 mM $[Fe(CN)_6]^{3-/4-}$ in 0.1 M KCl (dots represent the measured and the solid line represents the fitted EIS spectrum).

the pyrochlore clusters on the substrate electrode surface was somewhat poor, leading to their leaching. The leaching was visually noticeable already upon the addition of an electrolyte drop on the pyrochlore-modified SPCE surface before the measurement; thus, no further tests were carried out. The electrochemical behavior of APTES-$Bi_2Ru_2O_7$ clusters in 0.1 M KCl was different compared to the nonmodified $Bi_2Ru_2O_7$ clusters, with higher anodic currents for the OER reaction (Figure S4) and a signal for ORR that is separated from the hydrogen evolution reaction (HER) observed at more negative potentials. Importantly, the introduction of APTES resulted in a stable surface with no leaching, thus enabling its further investigation and modifications. Moreover, several advantageous characteristics were observed; i.e., the electrode modified with APTES-$Bi_2Ru_2O_7$ clusters exhibited a diffusion-controlled behavior in 1.0 mM $[Fe(CN)_6]^{3-/4-}$ in 0.1 M KCl characterized by a linear relationship between the peak current signals and the square root of the scan rate, fast electron transfer kinetics, and high redox reversibility (Figure 4a,b). Upon the modification with APTES, the APTES-$Bi_2Ru_2O_7$ clusters became firmly attached to the surface of the working SPCE, which was confirmed by running 30 consecutive CV (i_{pox} = 47.8 ± 0.3 μA, i_{pred} = −45.5 ± 0.3 μA) measurements in 1.0 mM $[Fe(CN)_6]^{3-/4-}$ in 0.1 M KCl (Figures 4c).

Notably, consecutive CV measurements showed that the leaching of the metallic ions from the APTES-$Bi_2Ru_2O_7$ clusters and valence interplay between the metallic centers were not observed. In addition, the obtained EIS spectra revealed almost metallic conductivity of the SPCE modified

https://doi.org/10.1021/acsami.4c17869
ACS Appl. Mater. Interfaces 2025, 17, 10792−10801

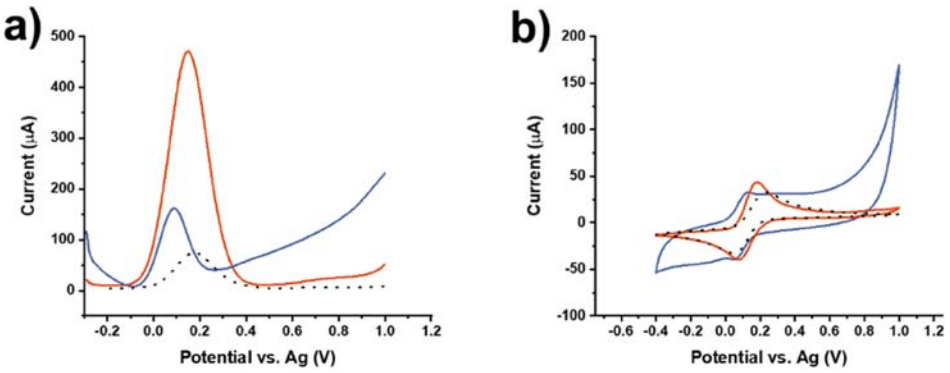

Figure 5. Superior behavior of APTES-$Bi_2Ru_2O_7$ clusters. (a) SWV and (b) CV measurements in 1.0 mM $[Fe(CN)_6]^{3-/4-}$ in 0.1 M KCl carried out on unmodified SPCE (black-dashed), APTES (blue), and APTES-$Bi_2Ru_2O_7$ cluster (red) modified SPCEs.

with APTES-$Bi_2Ru_2O_7$ clusters, with a small semicircle corresponding to the R_{ct} of ca. 180 Ω and a diffusion tail at lower frequencies (Figure 4d). The recorded spectra were fitted with a Randles-type equivalent circuit, shown in the inset of Figure 4d.

While the (electro)catalytic mechanism behind pyrochlore particles remains unsolved, it is hypothesized that pyrochlore reduces the kinetic barrier at active sites rather than engaging in electrochemical reactions with consumption, as demonstrated by Park et al.[7] For example, the same study showed that pyrochlore outperforms IrO_2 nanoparticles, despite the lower surface area. Indeed, in our study, the catalytic characteristics of $Bi_2Ru_2O_7$ pyrochlore were observed when comparing bare SPCE, APTES-modified SPCE, and SPCE modified with APTES-$Bi_2Ru_2O_7$ clusters (Figure 5). The SWV and CV measurements disclosed enhanced (electro)catalytic behavior of pyrochlore clusters reflected in a ca. 3-fold higher SWV response and well-defined reversible CV recording in 1.0 mM $[Fe(CN)_6]^{3-/4-}$ that was the external redox probe used also for all subsequent analytical performance tests.

Electrochemical studies proved favorable electrochemical and physical stability of the deposited APTES-$Bi_2Ru_2O_7$ clusters without any observable valence interplay of the metallic centers (Figures 4, 5, and S4). From the stability studies in Figure 4c, it is evident that electrode pretreatment with HNO_3 followed by APTES silanization of the $Bi_2Ru_2O_7$ pyrochlore clusters leads to mechanically stable binding of the electrocatalytic material on the SPCE surface via −OH groups introduced by the pretreatment. Most importantly, the $Bi_2Ru_2O_7$ clusters, in combination with APTES, yielded a substantial rise in the CV signal in the presence of an external redox probe, compared to the nonmodified electrodes and electrodes modified only with APTES (Figure 5). An explanation for this is that the oxygen vacancies facilitate the movement of electrons within the pyrochlore crystal lattice, similar to metal oxide semiconductors.[28] The existence of oxygen vacancies alters the electronic structure of pyrochlore materials, likely resulting in the formation of mid-gap states, acting as charge carriers.

Fabrication of the Immunosensor. The deposition of APTES-$Bi_2Ru_2O_7$ clusters on the SPCE substrate was followed by the immobilization of biorecognition elements. Efficient electrochemical immunosensing encompasses at least three key features, i.e., strong attachment of antibodies on the substrate electrode to minimize leaching, controlled site-specific binding to attain the desired orientation of the antibodies, and blockage of the nonspecific binding sites.[29] Protein A possesses a high affinity for the Fc region of IgG immunoglobulins, enabling their efficient immobilization; more importantly, its use provides proper orientation of the antibodies.[30,31] One protein A molecule has been shown to bind at least two molecules of IgG simultaneously.[32] Such an approach enhances the sensitivity and selectivity of the immunosensor by assuring that the active binding sites on the antibodies' Fab domains are readily accessible for the recognition event with the target spike protein. Notably, protein A can also serve as a blocking agent before using secondary antibodies in the case of immunohistochemistry to minimize nonspecific binding.[33] This implies that the presence of protein A within the immunosensing architecture may also contribute by blocking nonspecific binding to a certain extent, thereby further enhancing the selectivity and improving the signal-to-noise ratio of the immunosensor. Before the attachment of protein A, we introduced GA as the cross-linker, exhibiting immediate positive effects, such as a higher degree of reproducibility of further fabrication steps and the generation of a strong analytical signal toward SARS-CoV-2 spike protein. Stepwise fabrication of the immunosensor was monitored by EIS (Figure 6) using 1.0 mM $[Fe(CN)_6]^{3-/4-}$ in 0.1 M KCl as a redox probe. The impedimetric behavior of bare SPCE is characterized by one semicircle related to R_{ct} and a typical diffusion tail.

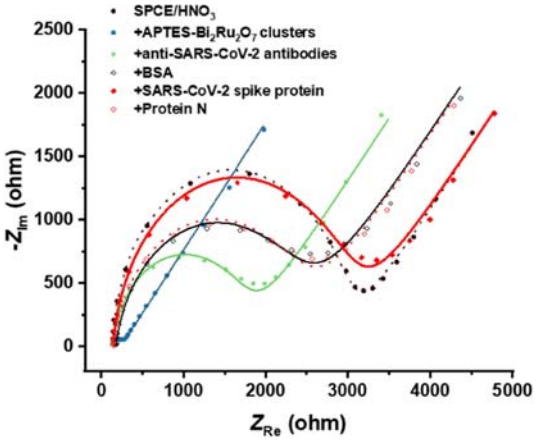

Figure 6. Step-by-step fabrication of the immunosensor. EIS (Nyquist) plots were recorded in 1.0 mM $[Fe(CN)_6]^{3-/4-}$ in 0.1 M KCl, along with the spike protein detection and negative control.

https://doi.org/10.1021/acsami.4c17869
ACS Appl. Mater. Interfaces 2025, 17, 10792−10801

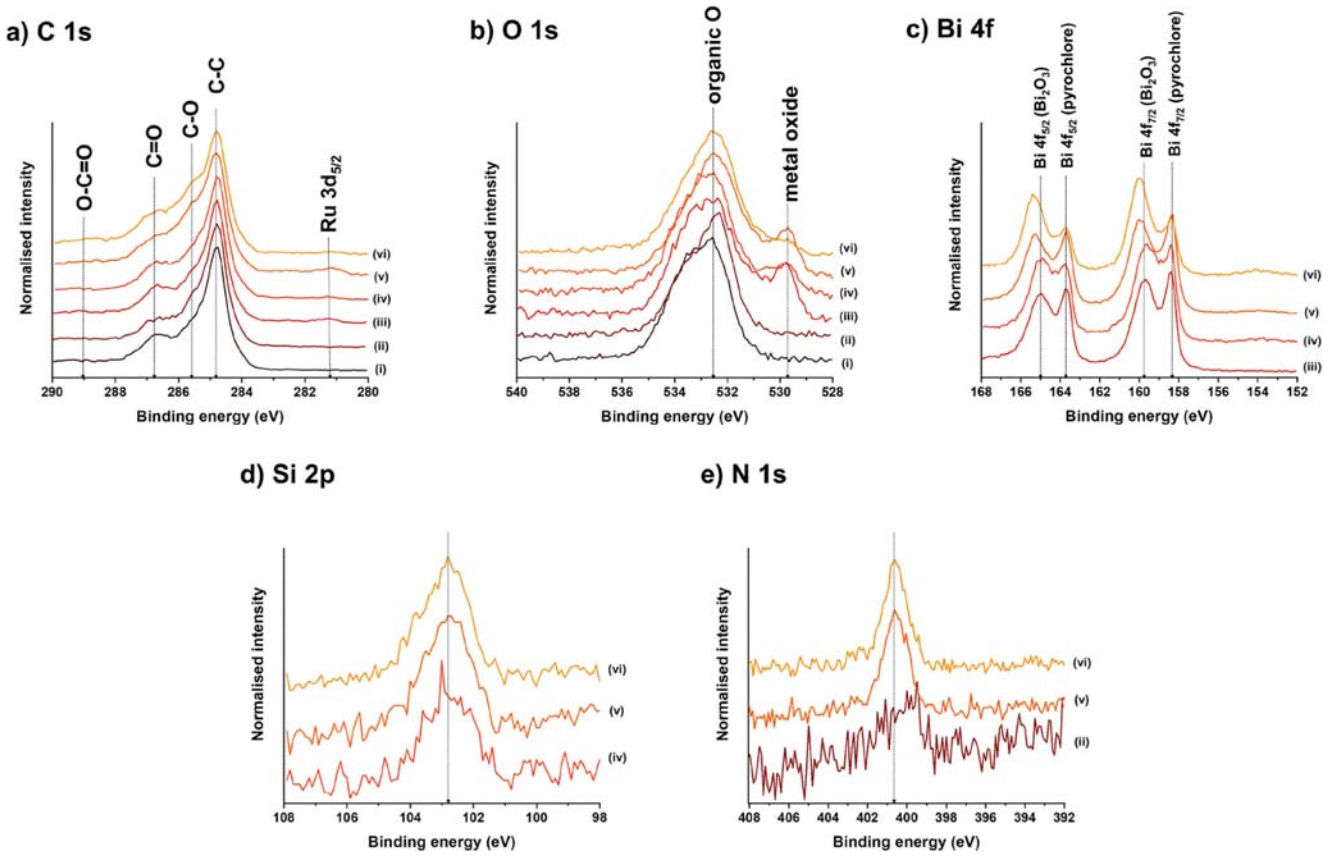

Figure 7. High-resolution XPS spectra for (a) C 1s and Ru 3d, (b) O 1s, (c) Bi 4f, (d) Si 2p, and (e) N 1s. The spectra were measured on different samples related to the gradual immunosensor fabrication: (i) bare SPCE, (ii) SPCE/HNO_3, (iii) SPCE/HNO_3/$Bi_2Ru_2O_7$, (iv) SPCE/HNO_3/APTES-$Bi_2Ru_2O_7$, (v) SPCE/HNO_3/APTES-$Bi_2Ru_2O_7$/GA/protein A, and (vi) SPCE/HNO_3/APTES-$Bi_2Ru_2O_7$/GA/protein A/anti-SARS-CoV-2 antibodies.

The introduction of APTES-$Bi_2Ru_2O_7$ clusters led to the system with the lowest R_{ct} and the prevailing diffusion pattern. After the immobilization of anti-SARS-CoV-2 antibodies via GA−protein A coupling, a higher R_{ct} value was observed. In the next step, the remaining nonspecific binding sites were blocked by adding BSA, and a further increase in R_{ct} characterized this surface modification. With this step, the fabrication of the immunosensor was completed. The other two signals shown in Figure 6 correspond to the negative control, i.e., incubation with protein N, showing a negligible difference versus the previous measurement, and a positive control, i.e., incubation with SARS-CoV-2 spike protein, demonstrating a significant increase in the R_{ct}. The relative change between R_{ct} before and after incubation with the spike protein was used as the analytical signal.

More insights into the fabrication process were acquired by using the XPS technique, with a particular emphasis on protein stacking (Figure 7). XPS analysis confirmed the presence of C, Ru, Bi, N, O, and Si on the surface throughout the immunosensor preparation steps. The survey spectra for all steps reveal the surface composition of each sample and are shown in Figure S5. The C 1s spectra for all samples include C−C, C−O, C═O, and C═O, located at 284.8, 285.6, 286.6, and 289.0 eV, respectively (Figure 7a). These features are visible and well pronounced in all samples, with a notable increase in the C−O signal upon adding protein species, i.e., protein A and anti-SARS-CoV-2 antibodies. The addition of $Bi_2Ru_2O_7$ clusters on the SPCE resulted in the formation of the Ru $3d_{5/2}$ signal located on the negative binding energy side of the C 1s spectra. Regarding the O 1s environment shown in Figure 7b (and Figure S6), several changes can be observed. Initially, the acidic treatment of SPCE resulted in a more pronounced C−OH feature at 532.3 eV. The addition of $Bi_2Ru_2O_7$ clusters introduced a metal oxide feature at 529.8 eV, which gradually decreased with the subsequent addition of proteins covering the $Bi_2Ru_2O_7$ moieties. Moreover, the Bi spectra shown in Figure 7c indicate two different environments of Bi, i.e., pyrochlore-related Bi $4f_{5/2}$ and Bi $4f_{7/2}$ features at 163.7 and 158.4 eV, respectively, along with Bi $4f_{5/2}$ and Bi $4f_{7/2}$ features at 165.0 and 159.7 eV, respectively, corresponding to Bi_2O_3.[34−38] The XPS analysis also revealed that after introducing proteins, the Bi $4f_{5/2}$ and Bi $4f_{7/2}$ peaks for pyrochlore decreased relative to Bi $4f_{5/2}$ and Bi $4f_{7/2}$ peaks for Bi_2O_3, suggesting that Bi_2O_3 had not been noticeably modified and that the pristine pyrochlore mostly accounts for further modification with APTES and subsequent protein stacking. The functionalization of clusters with APTES is evident in the spectra corresponding to the Si 2p feature (Figure 7d). As expected, no such peaks were observed for $Bi_2Ru_2O_7$ clusters without APTES (Figure S5), whereas APTES-$Bi_2Ru_2O_7$ clusters showed a strong feature at around 103.0 eV. This APTES-related signal remained present with the subsequent addition of protein A and anti-SARS-CoV-2 antibodies.

Finally, the N 1s environment, in both normalized (Figure 7e) and non-normalized (see Figure S6) spectra, is strongly associated with the protein content. The low-intensity peak

https://doi.org/10.1021/acsami.4c17869
ACS Appl. Mater. Interfaces 2025, 17, 10792−10801

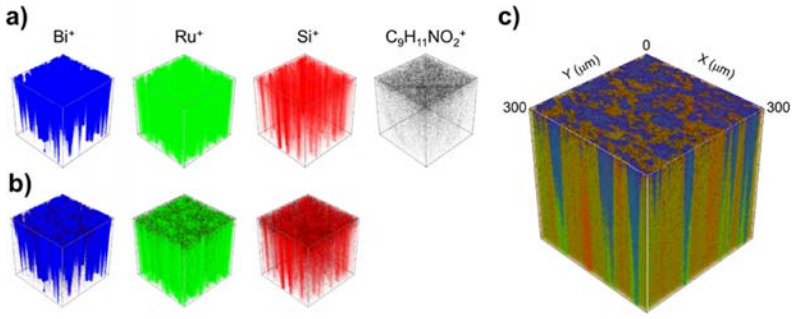

Figure 8. ToF-SIMS analysis of the immunosensing architecture. (a) 3D ToF-SIMS images showing the distribution of the main constituents, (b) an overlay of Bi^+ (blue), Ru^+ (green), and Si^+ (red) signals with the signal for $C_9H_{11}NO_2^+$ (black), and (c) an overlay of all signals to represent the complete immunosensor architecture.

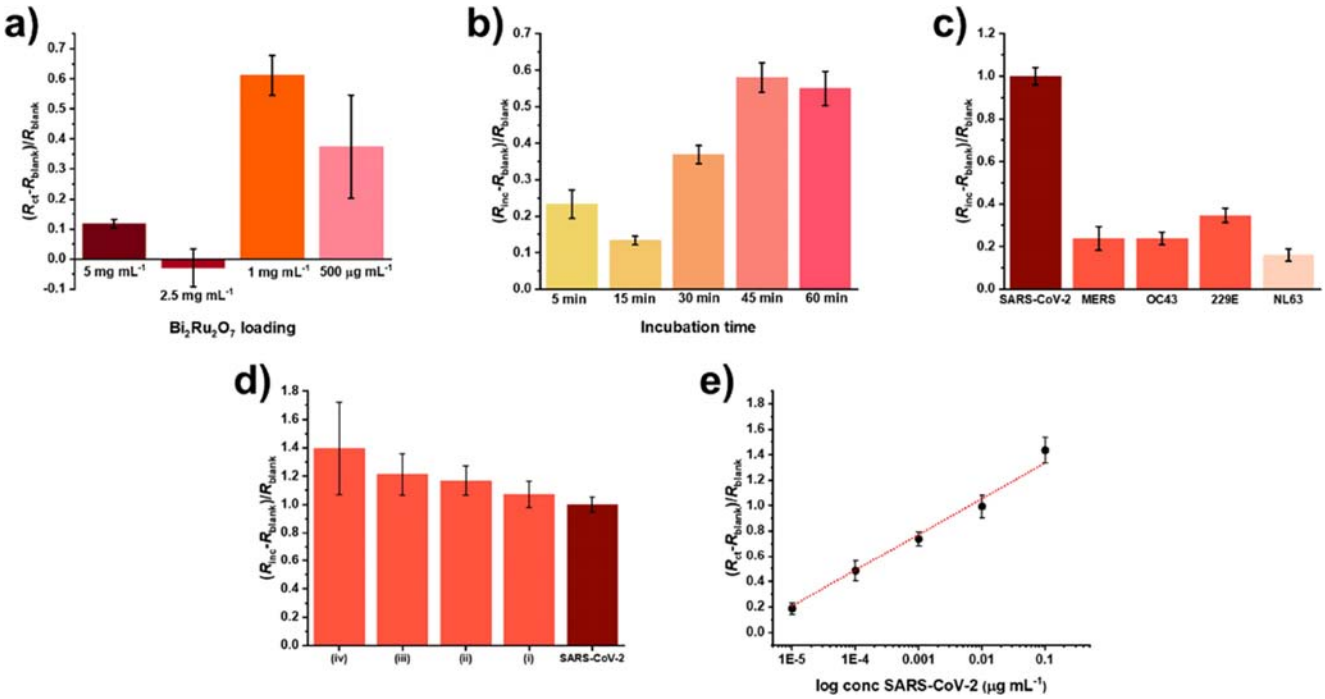

Figure 9. Optimization of the immunosensor and analytical performance. (a) Effect of the APTES-$Bi_2Ru_2O_7$ cluster loading on the EIS signal for 1 ng mL^{-1} SARS-CoV-2 spike protein in PBS, (b) optimization of the SARS-CoV-2 spike protein incubation time in PBS (1 ng mL^{-1} SARS-CoV-2 spike protein in PBS), (c) signals obtained in the presence of spike proteins of various coronaviruses in ANF (30 min incubation, 1 mg mL^{-1} APTES-$Bi_2Ru_2O_7$ loading, 1 ng mL^{-1} spike proteins), (d) signals obtained in the spike protein mixtures in ANF: (i) SARS-CoV-2 + MERS, (ii) SARS-CoV-2 + MERS + 229E, (iii) SARS-CoV-2 + MERS + 229E + NL63, (iv) SARS-CoV-2 + MERS + 229E + NL63 + OC43 (30 min incubation, 1 mg mL^{-1} of APTES-$Bi_2Ru_2O_7$ loading, 1 ng mL^{-1} spike proteins), and (e) calibration obtained using optimal operational conditions in ANF samples; the corresponding EIS Nyquist spectra are shown in Figure S9. All measurements were carried out using 1.0 mM $[Fe(CN)_6]^{3-/4-}$ in 0.1 M KCl.

observed in the sample for SPCE treated with nitric acid is attributed to the presence of NO_3^- residues. On the other hand, the progressive increase in N 1s signals in the XPS spectra with the addition of protein A and antibodies (along with the concurrent decrease of the Bi $4f_{5/2}$ and Bi $4f_{7/2}$ signals for pyrochlore) further confirmed the stacking of proteins on the pyrochlore clusters.

Along with the XPS, we performed a TOF-SIMS depth profiling analysis of the immunosensing architecture after the addition of anti-SARS-CoV-2 antibodies. The depth profiles of the signals characterizing different components for immunosensor construction are shown in Figure S7, while the 3D ToF-SIMS images showing the spatial distribution of components are presented in Figure 8. The immunosensor surface reveals a well-dispersed distribution of clusters, evidenced by both Ru^+ and Bi^+ signals, exhibiting an even surface coverage that is crucial for optimal functionality. The TOF-SIMS analysis further indicates that APTES closely follows the spatial distribution of these clusters, suggesting a uniform attachment across the surface. In addition, phenylalanine acts as a beacon for the proteins, i.e., the $C_9H_{11}NO_2^+$ moiety, facilitating their detection and interaction pattern. This amino acid is ubiquitously present on the immunosensor, as shown in Figure 8a, separately and with respect to Bi^+, Ru^+, and Si^+ signals; the overlay ToF-SIMS 3D image is depicted in Figure 8b. Another identification of proteins on the topmost position (ToF-SIMS has an analyzed sampling depth of about 2 nm) comes from the presence of the signal for S^- corresponding to

https://doi.org/10.1021/acsami.4c17869
ACS Appl. Mater. Interfaces 2025, 17, 10792−10801

cysteine residues, which are confirmed through the analysis in negative ToF-SIMS polarity, as illustrated in Figure S8.

Analytical Performance of the Impedimetric Immunosensor. To study the effect of different $Bi_2Ru_2O_7$ pyrochlore loadings on the SPCE surface, we applied different pyrochlore modification solutions, i.e., 0.5, 1.0, 2.5, and 5.0 mg mL^{-1}, and followed the signal for 1.0 ng mL^{-1} of the SARS-CoV-2 spike protein. The signals significantly decreased at higher concentrations of 2.5 and 5.0 mg mL^{-1} pyrochlore, whereas the concentration of 1 mg mL^{-1} was selected as optimal (Figure 9a). The superior electroanalytical performances at 1.0 and 0.5 mg mL^{-1} of APTES-$Bi_2Ru_2O_7$ clusters can be attributed to several factors. At these concentrations, the pyrochlore is well-dispersed over the supporting SPCE, maximizing the active surface area available for the interaction with the GA cross-linker and the functional proteins, as shown in Figure S9. This uniformity ensures efficient electron transfer and enhances the electrochemical response of the immunosensor. In contrast, at higher concentrations of 2.5 and 5.0 mg mL^{-1} APTES-$Bi_2Ru_2O_7$ clusters, the (electro)catalytic material aggregates, leading to less uniform deposition. Such aggregation can result in a reduced effective surface area, hindering the electron transfer process and thus diminishing the analytical signal. In addition, we evaluated five different incubation times of the SARS-CoV-2 spike protein, i.e., 5, 15, 30, 45, and 60 min, to identify the duration yielding the highest response (Figure 9b). While a 5 min incubation time produced a slightly higher signal than a 15 min incubation, signal height significantly increased at 30 min incubation and at longer incubation times. Notably, the signal reached a maximum after 45 min incubation, with a minimal decrease observed after 60 min incubation. The incubation time study suggests that the binding interaction between the target protein and the immunosensor improves with a longer incubation time up to a certain point. The maximum signal observed after 45 min incubation indicates that the binding sites of the immunosensor surface have likely become saturated with the analyte protein. However, from a practical perspective, the 30 min incubation time represents an optimal balance between attaining a satisfactorily high electroanalytical signal and maintaining a reasonable assay duration. Shorter incubation times, such as 5 or 15 min, may not allow sufficient protein binding, leading to suboptimal immunosensing performance. To assess the selectivity of the optimized immunosensor toward SARS-CoV-2, we conducted measurements using spike proteins from various coronaviruses and their combinations, including MERS-CoV, HCoV-229E, HCoV-NL63, and HCoV-OC43 (Figures 9c,d).

The results proved that the immunosensor exhibited good selectivity for SARS-CoV-2, as evidenced by the considerably highest electroanalytical signal compared with the other coronaviruses, although a certain degree of interference could be observed for all tested proteins. Such performances can be attributed to an effective match between the selected antibody−antigen pair, alongside the efficient immobilization of the antibodies and blocking of the nonspecific binding sites. The relatively low interference observed for the selected HCoV spike proteins can be attributed to the similarity of structural motifs, such as the HCoV-229E spike protein, which may cause cross-reactivity with anti-SARS-CoV-2 antibodies. Although the RBD domains of all coronaviruses are different, similarities in other regions of the S1 subunit could result in a partial binding affinity. All measurements were performed in triplicate against the 1 ng mL^{-1} SARS-CoV-2 spike protein in ANF.

Finally, the immunosensor's performance was tested across a wide concentration range of 10^{-5}−10^{-1} μg mL^{-1} (corresponding to 130 fM to 1.3 nM) SARS-CoV-2 spike protein in ANF, as evidenced by the resulting linear calibration curve with a correlation coefficient (r^2) of 0.98 (Figure 9e). Each calibration point, including blanks, was measured in four replicates using four identically prepared immunosensors per measuring point.

Apart from a wide operational concentration range, the optimized immunosensor exhibited a low detection limit (3σ criterion) of only 118 fM obtained in ANF with a relatively complex matrix. These results are competitive or surpass the performances of many reported impedimetric biosensors for the detection of the spike protein, including gold electrode incorporating a specific peptide capture probe with the detection limit of 1.28 nM,[39] multiwalled carbon nanotubes functionalized with methylene blue on SPCE with the detection limit of 0.255 nM,[40] ACE2 or CD147 functionalized screen-printed gold electrodes with the detection limit of 0.498 nM,[41] electrodeposited gold nanoparticles functionalized with mercaptoacetic acid monolayers on the supporting SPCE with the detection limit of 3.16 pM,[42] V_2CT_x MXene-based immunosensors developed by our group with the detection limit of 45 fM in PBS,[43] screen-printed gold electrode incorporating the chicken IgY antispike antibody with the detection limit of 72.2 fM in PBS,[44] or SPCE modified with the metal−organic framework and silica with the detection limit of 1.27 fM in a nasal sample.[45]

CONCLUSIONS

In this work, we demonstrate the synergistic effects of the (electro)catalytic nature of pyrochlore, the suitable stabilization and immobilization of pyrochlore by APTES, and the ability of APTES-modified $Bi_2Ru_2O_7$ clusters as efficient domains for stacking functional proteins to develop a highly sensitive and selective immunosensor. CV and SWV measurements revealed improved electrochemical and physical stability of the APTES-$Bi_2Ru_2O_7$ clusters without any observable valence interplay between the Ru and Bi centers. Presumably, this electrochemical activity is due to oxygen deficiency and metallic-like conductivity, which contributes to the increase of electron pathways for the external redox reaction, the introduction of additional active sites, and facilitating electron transfer. After stacking protein A and antibodies, the immunosensor exhibited high selectivity, owing to effective matching between the selected antibody−antigen pair, along with the efficient immobilization of the antibodies and blocking of the nonspecific binding sites. The high sensitivity and overall electroanalytical performance, characterized by high linearity in the investigated concentration range and a detection limit of 118 fM SARS-CoV-2 spike protein, underline the advantageous application of pyrochlores in the development of high-performance immunosensors.

MATERIALS AND METHODS

Synthesis and Characterization of $Bi_2Ru_2O_7$. A stoichiometric mixture of α-Bi_2O_3 (Fluka, 99.8%) and $RuO_2 \times H_2O$ (Acros Organics, >54% Ru) was dry homogenized for about 30 min in an agate mortar, heated at 900 °C for 3 h (heating rate 4 °C min^{-1}) in an open Pt-crucible in a chamber furnace, and then cooled down to room temperature. The obtained powder was examined on an Ital Structure APD 2000 X-ray powder diffractometer using Cu $K\alpha$ radiation (λ =

https://doi.org/10.1021/acsami.4c17869
ACS Appl. Mater. Interfaces 2025, 17, 10792−10801

1.5418 Å) in the 2θ range from 20 to 80° with a step width of 0.02° and a counting time of 1 s per step.

FE-SEM images and EDX analysis of pyrochlore clusters deposited on the SPCE surface were obtained with a high-resolution scanning electron microscope (Carl Zeiss SUPRA 35 VP FE-SEM) equipped with an energy-dispersive X-ray spectrometer (Oxford Instruments Inca 400 EDX). Bare and SPCEs modified with APTES-$Bi_2Ru_2O_7$ clusters were subjected to optical inspection using 3D profilometry (Zegage PRO HR, Zygo Corporation, PA).

X-ray photoelectron spectroscopy (XPS) analyses were conducted using a Supra+ system from Kratos (Manchester, UK) with an Al K_α source as the excitation source. The spectra were referenced by aligning the C−C/C-H peak in the C 1s to 284.8 eV. The SPCEs were mounted on the sample holder by using double-sided carbon tape. Measurements were conducted at a takeoff angle of 90°, focusing on a spot size of 300 × 700 μm, with the pass energy set at 20 eV. ESCApe 1.5 software from Kratos was utilized for data collection and analysis.

For the ToF-SIMS experiments, an M6 instrument from Iontof (Münster, Germany) was utilized to perform the measurements. The primary ion beam used was a Bi^+ beam with an energy of 30 keV and the target current set at 1.0 pA. Surface Lab 7.3 software, provided by Iontof, was employed for both data acquisition and analysis. Calibration of the spectra was achieved by referencing known ion signals at specific m/z values. To address any potential charging issues during the measurements, a flood gun was turned on. Silicon-free double-sided tape was used to secure SPCEs onto a top-mounted sample holder. Depth profiling was carried out using 250 kV Cs^+ ions, operating at a target current of 10 nA. The sputter area was 500 by 500 μm, and the analysis was performed within the center of the sputter crater, targeting a spot size of 300 by 300 μm.

Immunosensor Fabrication. The working electrode of the SPCE (Metrohm, DRP-110, d = 4 mm, shown in Figures S1 and S10) was treated with 0.5 M HNO_3 for 15 min to activate its surface by introducing −OH groups. Afterward, the electrode was rinsed with ultrapure H_2O and dried with nitrogen under a mild gas flow. Then, 10 μL of APTES-modified $Bi_2Ru_2O_7$ powder was applied to the working electrode by drop-casting and left at 35 °C for 1 h to dry completely. Previously, the APTES-$Bi_2Ru_2O_7$ clusters were prepared using the following procedure: the synthesized $Bi_2Ru_2O_7$ was dispersed in absolute ethanol to form a 5 mg mL^{-1} suspension followed by adding 5 vol % of APTES. After 2 h of vigorous stirring at room temperature, the mixture was centrifuged twice for 3 min at 11000 rpm while rinsing with absolute ethanol. After the second centrifugation, followed by rinsing, the activated powder was resuspended in distilled H_2O to make a 5 mg mL^{-1} solution. The working electrode modified with APTES-$Bi_2Ru_2O_7$ clusters was covered with 10 μL of PBS (pH 7.4) containing 5% GA, and the electrode was left at 4 °C for 2 h to promote the formation of the GA cross-link. Then, the electrode was rinsed by immersion into distilled H_2O for 10 s and dried under a mild nitrogen gas flow. This was followed by covering the electrode with 10 μL of 5 μg mL^{-1} protein A in PBS (pH 7.4) and left for 1 h at room temperature (22−25 °C) under dark storage conditions. The electrode was then rinsed with distilled H_2O, dried with nitrogen, and incubated with 10 μL of 10 μg mL^{-1} anti-SARS-CoV-2 antibodies in PBS (pH 7.4) for 1 h at room temperature. To minimize the nonspecific binding, the remaining cross-links and other nonspecific binding sites were blocked by adding 10 μL of 100 μg mL^{-1} BSA solution in PBS (pH 7.4) on the working electrode and left at room temperature for 1 h. After a short rinsing sequence with Tris buffer, the immunosensor was dried with nitrogen and was ready for use. The complete fabrication procedure is depicted in Scheme S1.

Electrochemical Measurements. All measurements were carried out using a portable PalmSens 4 potentiostat/galvanostat operated by PSTrace 5.9 (PalmSens BV, The Netherlands). Electrochemical impedance spectroscopy (EIS) was carried out in a frequency range of 10^4−10^{-1} Hz at the potential of +0.14 V vs a screen-printed quasi-reference silver electrode and an amplitude of 5 mV in solution containing 1.0 mM $[Fe(CN)_6]^{3-/4-}$ in 0.1 M KCl as a redox probe. The recorded EIS spectra were fitted using the equivalent electrical circuit $R_S([R_{ct}Z_W]Q_{dl})$. Here, R_S corresponds to the solution resistance, R_{ct} is the charge transfer resistance of the outer sensing layer, Z_W is a Warburg element that models the diffusion phenomena, and Q_{dl} is a constant phase element used to model nonideal double-layer capacitance.

■ ASSOCIATED CONTENT

Supporting Information

The Supporting Information is available free of charge at https://pubs.acs.org/doi/10.1021/acsami.4c17869.

Chemicals, preparation of buffer solutions, fabrication of the immunosensor; Scheme S1, immunosensor fabrication protocol; Figure S1, 3D interferometry image of SPCE; Figure S2, FE-SEM image of the APTES-$Bi_2Ru_2O_7$ cluster; Figure S3, EDX analysis of APTES-$Bi_2Ru_2O_7$ clusters; Figure S4, cyclic voltammograms of modified SPCEs; Figure S5, XPS survey spectra; Figure S6, non-normalized XPS spectra for N 1s and O 1s; Figure S7, depth profiles measured in positive-ion TOF-SIMS polarity; Figure S8, detailed negative-ion ToF-SIMS spectrum showing the S^- signal; Figure S9, EIS Nyquist spectra for different concentrations of the SARS-CoV-2 spike protein in ANF; and Figure S10, 3D and 2D interferometry images of bare and APTES-$Bi_2Ru_2O_7$-modified SPCEs (PDF)

■ AUTHOR INFORMATION

Corresponding Authors

Nikola Tasić − *Department of Analytical Chemistry, National Institute of Chemistry, 1000 Ljubljana, Slovenia;* orcid.org/0000-0002-0582-2252; Email: nikola.tasic@ki.si

Samo B. Hočevar − *Department of Analytical Chemistry, National Institute of Chemistry, 1000 Ljubljana, Slovenia;* orcid.org/0000-0003-2980-4822; Email: samo.hocevar@ki.si

Authors

Nika Vranešič − *Department of Analytical Chemistry, National Institute of Chemistry, 1000 Ljubljana, Slovenia*

Dino Metarapi − *Department of Analytical Chemistry, National Institute of Chemistry, 1000 Ljubljana, Slovenia*

Kristina Mervič − *Department of Analytical Chemistry, National Institute of Chemistry, 1000 Ljubljana, Slovenia;* orcid.org/0009-0006-5000-3201

Milan Žunić − *University of Belgrade, Institute for Multidisciplinary Research, 11030 Belgrade, Serbia*

Aleksandra Dapčević − *Department of General and Inorganic Chemistry, Faculty of Technology and Metallurgy, University of Belgrade, 11000 Belgrade, Serbia*

Matjaž Finšgar − *Faculty of Chemistry and Chemical Engineering, University of Maribor, 2000 Maribor, Slovenia;* orcid.org/0000-0002-8302-9284

Complete contact information is available at: https://pubs.acs.org/10.1021/acsami.4c17869

Author Contributions

N.T. conceptualized the research idea, designed the study, analyzed the data, and wrote the manuscript. N.V. carried out the electrochemical studies, immunosensor fabrication, and analytical performance tests and assisted with data analysis. A.D. and M.Ž. optimized the synthetic method for $Bi_2Ru_2O_7$,

https://doi.org/10.1021/acsami.4c17869
ACS Appl. Mater. Interfaces 2025, 17, 10792−10801

synthesized the pyrochlore clusters, performed the XRD analysis, and contributed to the discussion of the (electro)-catalytic material characterization. D.M. performed FE-SEM, EDX, and 3-D profilometry analyses. K.M. performed 3-D profilometry analyses. M.F. conducted XPS and TOF-SiMS analyses, contributed to interpreting the obtained data, and provided theoretical understanding. S.B.H. provided the funding for the research, assisted with the study design, and wrote the manuscript. The manuscript has inputs from all authors.

Notes

The authors declare no competing financial interest.

■ ACKNOWLEDGMENTS

This research received funding from the Slovenian Research Agency (Research Programs P1-0034 and P2-0118, and Research Project J1-4416) and the Ministry of Science, Technological Development and Innovation of the Republic of Serbia (Contract No. 451-03-65/2024-03/200135 and Contract No. 451-03-66/2024-03/200053). The project was co-financed by the Republic of Slovenia, the Ministry of Higher Education, Science and Innovation, and the European Union under the European Regional Development Fund.

■ REFERENCES

(1) Longo, J. M.; Raccah, P. M.; Goodenough, J. B. $Pb_2M_2O_{7-x}$ (M = Ru, Ir, Re) — Preparation and Properties of Oxygen Deficient Pyrochlores. *Mater. Res. Bull.* **1969**, *4* (3), 191−202.

(2) Bouchard, R. J.; Gillson, J. L. A New Family of Bismuth — Precious Metal Pyrochlores. *Mater. Res. Bull.* **1971**, *6* (8), 669−679.

(3) Hrovat, M.; Belavič, D.; Samardžija, Z. Temperature Sensors Made by Combinations of Some Standard Thick Film Materials. *J. Mater. Sci. Lett.* **2000**, *19*, 651−655.

(4) Hrovat, M.; Jan, F.; Kolar, D. The Interaction Between Thick Film Conductors and Low Ohmic Resistors. *Microelectronics International* **1986**, *3* (2), 14−15.

(5) Dziedzic, A.; Golonka, L. Electrical Properties of Conductive Materials Used in Thick-Film Resistors. *J. Mater. Sci.* **1988**, *23* (9), 3151−3155.

(6) Kuž, R.; Kopřivová, E.; Broukal, J. Thick Film Resistors with High TCR. *Microelectronics International* **1987**, *4* (1), 28−31.

(7) Park, J.; Jang, H.; Lee, S. Y.; Jeon, J. S.; Kim, M. G. Redox Reaction Does Not Facilitate Oxygen Evolution on Bismuth Ruthenate Pyrochlore. *J. Mater. Chem. A Mater.* **2022**, *10* (2), 561−569.

(8) Kim, M.; Ju, H.; Kim, J. Single Crystalline $Bi_2Ru_2O_7$ Pyrochlore Oxide Nanoparticles as Efficient Bifunctional Oxygen Electrocatalyst for Hybrid Na-Air Batteries. *Chemical Engineering Journal* **2019**, *358*, 11−19.

(9) Esposito, V.; Luong, B. H.; Di Bartolomeo, E.; Wachsman, E. D.; Traversa, E. Applicability of $Bi_2Ru_2O_7$ Pyrochlore Electrodes for ESB and BIMEVOX Electrolytes. *J. Electrochem. Soc.* **2006**, *153* (12), A2232.

(10) Takeda, T.; Kanno, R.; Kawamoto, Y.; Takeda, Y.; Yamamoto, O. New Cathode Materials for Solid Oxide Fuel Cells Ruthenium Pyrochlores and Perovskites. *J. Electrochem. Soc.* **2000**, *147* (5), 1730.

(11) Bamiduro, G. J.; Zahran, E. M. $Pd@Bi_2Ru_2O_7/BiVO_4$ Z-Scheme Heterojunction Nanocomposite Photocatalyst for the Degradation of Trichloroethylene. *ACS Appl. Mater. Interfaces* **2023**, *15* (51), 59337−59347.

(12) Shimizu, Y.; Nishi, H.; Suzuki, H.; Maeda, K. Solid-State NOx Sensor Combined with NASICON and Pb−Ru-Based Pyrochlore-Type Oxide Electrode. *Sens Actuators B Chem.* **2000**, *65* (1−3), 141−143.

(13) Kaushik, A. K.; Dhau, J. S.; Gohel, H.; Mishra, Y. K.; Kateb, B.; Kim, N.-Y.; Goswami, D. Y. Electrochemical SARS-CoV-2 Sensing at Point-of-Care and Artificial Intelligence for Intelligent COVID-19 Management. *ACS Appl. Bio Mater.* **2020**, *3* (11), 7306−7325.

(14) Mao, S.; Fu, L.; Yin, C.; Liu, X.; Karimi-Maleh, H. The Role of Electrochemical Biosensors in SARS-CoV-2 Detection: A Bibliometrics-Based Analysis and Review. *RSC Adv.* **2022**, *12* (35), 22592−22607.

(15) Zambry, N. S.; Obande, G. A.; Khalid, M. F.; Bustami, Y.; Hamzah, H. H.; Awang, M. S.; Aziah, I.; Manaf, A. A. Utilizing Electrochemical-Based Sensing Approaches for the Detection of SARS-CoV-2 in Clinical Samples: A Review. *Biosensors (Basel)* **2022**, *12* (7), 473.

(16) Karakuş, E.; Erdemir, E.; Demirbilek, N.; Liv, L. Colorimetric and Electrochemical Detection of SARS-CoV-2 Spike Antigen with a Gold Nanoparticle-Based Biosensor. *Anal. Chim. Acta* **2021**, *1182*, No. 338939.

(17) Alam, A.; Uppal, T.; Islam, M. S.; Misra, M.; Verma, S. C. Polyaniline/Titania Nanotube-Based Biosensor Strip for Sensitive and Specific Electrochemical Detection of SARS-CoV-2. *ACS Omega* **2023**, *8* (48), 45700−45707.

(18) Adeel, M.; Asif, K.; Canzonieri, V.; Barai, H. R.; Rahman, Md. M.; Daniele, S.; Rizzolio, F. Controlled, Partially Exfoliated, Self-Supported Functionalized Flexible Graphitic Carbon Foil for Ultrasensitive Detection of SARS-CoV-2 Spike Protein. *Sens Actuators B Chem.* **2022**, *359*, No. 131591.

(19) Chen, W. Y.; Lin, H.; Barui, A. K.; Gomez, A. M. U.; Wendt, M. K.; Stanciu, L. A. DNA-Functionalized $Ti_3C_2T_x$ MXenes for Selective and Rapid Detection of SARS-CoV-2 Nucleocapsid Gene. *ACS Appl. Nano Mater.* **2022**, *5* (2), 1902−1910.

(20) Malla, P.; Liu, C.-H.; Wu, W.-C.; Kabinsing, P.; Sreearunothai, P. Synthesis and Characterization of Au-Decorated Graphene Oxide Nanocomposite for Magneto-Electrochemical Detection of SARS-CoV-2 Nucleocapsid Gene. *Talanta* **2023**, *262*, No. 124701.

(21) Alafeef, M.; Moitra, P.; Dighe, K.; Pan, D. RNA-Extraction-Free Nano-Amplified Colorimetric Test for Point-of-Care Clinical Diagnosis of COVID-19. *Nat. Protoc* **2021**, *16* (6), 3141−3162.

(22) Zhou, Y.; Wu, Y.; Ding, L.; Huang, X.; Xiong, Y. Point-of-Care COVID-19 Diagnostics Powered by Lateral Flow Assay. *TrAC Trends in Analytical Chemistry* **2021**, *145*, No. 116452.

(23) Teymouri, M.; Mollazadeh, S.; Mortazavi, H.; Naderi Ghalenoie, Z.; Keyvani, V.; Aghababaei, F.; Hamblin, M. R.; Abbaszadeh-Goudarzi, G.; Pourghadamyari, H.; Hashemian, S. M. R.; Mirzaei, H. Recent Advances and Challenges of RT-PCR Tests for the Diagnosis of COVID-19. *Pathol Res. Pract* **2021**, *221*, No. 153443.

(24) Rezaei, M.; Razavi Bazaz, S.; Morshedi Rad, D.; Shimoni, O.; Jin, D.; Rawlinson, W.; Ebrahimi Warkiani, M. A Portable RT-LAMP/CRISPR Machine for Rapid COVID-19 Screening. *Biosensors (Basel)* **2021**, *11* (10), 369.

(25) Umar Ibrahim, A.; Pwavodi, P. C.; Ozsoz, M.; Al-Turjman, F.; Galaya, T.; Agbo, J. J. Crispr Biosensing and Ai Driven Tools for Detection and Prediction of Covid-19. *Journal of Experimental & Theoretical Artificial Intelligence* **2023**, *35* (4), 489−505.

(26) Yamamoto, T.; Kanno, R.; Takeda, Y.; Yamamoto, O.; Kawamoto, Y.; Takano, M. Crystal Structure and Metal-Semiconductor Transition of the $Bi_{2-X}Ln_xRu_2O_7$ Pyrochlores (Ln = Pr-Lu). *J. Solid State Chem.* **1994**, *109* (2), 372−383.

(27) Kennedy, B. J. Oxygen Vacancies in Pyrochlore Oxides: Powder Neutron Diffraction Study of $Pb_2Ir_2O_{6.5}$ and $Bi_2Ir_2O_{7-y}$. *J. Solid State Chem.* **1996**, *123* (1), 14−20.

(28) Zhang, C.; Liu, G.; Geng, X.; Wu, K.; Debliquy, M. Metal Oxide Semiconductors with Highly Concentrated Oxygen Vacancies for Gas Sensing Materials: A Review. *Sens Actuators A Phys.* **2020**, *309*, No. 112026.

(29) Gao, S.; Guisán, J. M.; Rocha-Martin, J. Oriented Immobilization of Antibodies onto Sensing Platforms - A Critical Review. *Anal. Chim. Acta* **2022**, *1189*, No. 338907.

(30) Kengne-Momo, R. P.; Lagarde, F.; Daniel, P.; Pilard, J. F.; Durand, M. J.; Thouand, G. Polythiophene Synthesis Coupled to Quartz Crystal Microbalance and Raman Spectroscopy for Detecting Bacteria. *Biointerphases* **2012**, *7* (1−4), 67.

https://doi.org/10.1021/acsami.4c17869
ACS Appl. Mater. Interfaces 2025, 17, 10792−10801

(31) Suzuki, M.; Ozawa, F.; Sugimoto, W.; Aso, S. Miniature Surface-Plasmon Resonance Immunosensors–Rapid and Repetitive Procedure. *Anal Bioanal Chem.* **2002**, *372* (2), 301−304.
(32) Yang, L.; Biswas, M. E.; Chen, P. Study of Binding between Protein A and Immunoglobulin G Using a Surface Tension Probe. *Biophys. J.* **2003**, *84* (1), 509−522.
(33) Sørensen, O.; Arnljots, K.; Cowland, J. B.; Bainton, D. F.; Borregaard, N. The Human Antibacterial Cathelicidin, HCAP-18, Is Synthesized in Myelocytes and Metamyelocytes and Localized to Specific Granules in Neutrophils. *Blood* **1997**, *90* (7), 2796−2803.
(34) Shukla, A. K.; Kannan, A. M.; Hegde, M. S.; Gopalakrishnan, J. Effect of Counter Cations on Electrocatalytic Activity of Oxide Pyrochlores towards Oxygen Reduction/Evolution in Alkaline Medium: An Electrochemical and Spectroscopic Study. *J. Power Sources* **1991**, *35* (2), 163−173.
(35) Dharmadhikari, V. S.; Sainkar, S. R.; Badrinarayan, S.; Goswami, A. Characterisation of Thin Films of Bismuth Oxide by X-Ray Photoelectron Spectroscopy. *J. Electron Spectrosc. Relat. Phenom.* **1982**, *25* (2), 181−189.
(36) Felthouse, T. Expanded Lattice Ruthenium Pyrochlore Oxide Catalysts II. Catalyst Surface Investigations by Electron Microscopy, X-Ray Photoelectron Spectroscopy, and Temperature-Programmed Reduction and Oxidation. *J. Catal.* **1991**, *127* (1), 421−444.
(37) Cox, P. A.; Goodenough, J. B.; Tavener, P. J.; Telles, D.; Egdell, R. G. The Electronic Structure of $Bi_{2-x}Gd_xRu_2O_7$ and RuO_2: A Study by Electron Spectroscopy. *J. Solid State Chem.* **1986**, *62* (3), 360−370.
(38) Gai, X.; Qu, J.; Zhang, N.; You, C.; Zhang, F.; Lv, T.; Tao, Q.; Zhu, P.; Li, Y.; Wang, X. Pressure-Induced Suppression of Static Disorder and Lattice Distortion in Pyrochlore $Bi_2Ru_2O_7$. *J. Phys. Chem. C* **2024**, *128* (17), 7306−7315.
(39) Wolfe, M.; Webb, S.; Chushak, Y.; Krabacher, R.; Liu, Y.; Swami, N.; Harbaugh, S.; Chávez, J. A High-Throughput Pipeline for Design and Selection of Peptides Targeting the SARS-Cov-2 Spike Protein. *Sci. Rep* **2021**, *11* (1), 21768.
(40) Tortolini, C.; Angeloni, A.; Antiochia, R. A Comparative Study of Voltammetric vs impedimetric Immunosensor for Rapid SARS-CoV-2 Detection at the Point-of-care. *Electroanalysis* **2023**, *35* (4), No. e202200349.
(41) Tepeli Büyüksünetçi, Y.; Çitil, B. E.; Anık, Ü. An impedimetric Approach for COVID-19 Detection. *Analyst* **2021**, *147* (1), 130−138.
(42) Brazaca, L. C.; Imamura, A. H.; Gomes, N. O.; Almeida, M. B.; Scheidt, D. T.; Raymundo-Pereira, P. A.; Oliveira, O. N.; Janegitz, B. C.; Machado, S. A. S.; Carrilho, E. Electrochemical Immunosensors Using Electrodeposited Gold Nanostructures for Detecting the S Proteins from SARS-CoV and SARS-CoV-2. *Anal Bioanal Chem.* **2022**, *414* (18), 5507−5517.
(43) Tasić, N.; Konjević, I.; Lobato, A.; Metarapi, D.; Finšgar, M.; Oliveira, F. M.; Sofer, Z.; Gusmão, R.; Zhang, X.; Hočevar, S. B. Study of V_2CT_x -MXene Based Immunosensor for Sensitive Label-Free impedimetric Detection of SARS-CoV-2 Spike Protein. *ACS Appl. Mater. Interfaces* **2024**, *16*, 30196.
(44) Al-Qaoud, K. M.; Obeidat, Y. M.; Al-Omari, T.; Okour, M.; Al-Omari, M. M.; Ahmad, M. I.; Alshadfan, R.; Rawashdeh, A. M. The Development of an Electrochemical Immunosensor Utilizing Chicken IgY Anti-Spike Antibody for the Detection of SARS-CoV-2. *Sci. Rep* **2024**, *14* (1), 748.
(45) Mehmandoust, M.; Gumus, Z. P.; Soylak, M.; Erk, N. Electrochemical Immunosensor for Rapid and Highly Sensitive Detection of SARS-CoV-2 Antigen in the Nasal Sample. *Talanta* **2022**, *240*, No. 123211.

https://doi.org/10.1021/acsami.4c17869
ACS Appl. Mater. Interfaces 2025, 17, 10792−10801